Thermally induced nanoscale structural and morphological changes for atomic-layer-deposited Pt on $SrTiO_3$(001)

Zhenxing Feng,[1] Steven T. Christensen,[1] Jeffrey W. Elam,[2] Byeongdu Lee,[3] Mark C. Hersam,[1,4] and Michael J. Bedzyk[1,5,6,a)]

[1]*Department of Materials Science and Engineering, Northwestern University, Evanston, Illinois 60208, USA*
[2]*Energy Systems Division, Argonne National Laboratory, Argonne, Illinois 60439, USA*
[3]*X-ray Science Division, Argonne National Laboratory, Argonne, Illinois 60439, USA*
[4]*Department of Chemistry, Northwestern University, Evanston, Illinois 60208, USA*
[5]*Department of Physics and Astronomy, Northwestern University, Evanston, Illinois 60208, USA*
[6]*Materials Science Division, Argonne National Laboratory, Argonne, Illinois 60439, USA*

(Received 30 September 2010; accepted 26 April 2011; published online 30 November 2011)

Platinum grown by atomic layer deposition (ALD) on $SrTiO_3$(001) surfaces was studied as a function of Pt coverage and post-deposition thermal treatment. The combination of atomic-force microscopy, scanning electron microscopy, x-ray fluorescence, x-ray reflectivity, and grazing-incidence small-angle x-ray scattering reveals significant changes in the nanoscale surface morphology and crystallinity for the differently prepared films. Surfaces with Pt coverages from 1 to 40 monolayers (ML) show different initial morphologies that evolve into different final Pt microstructures after annealing to 800 °C. These distinct nanoscale structural changes are explained by surface diffusion and the surface and interface energies for noble metals on oxides. © *2011 American Institute of Physics*. [doi:10.1063/1.3661163]

I. INTRODUCTION

Metallic thin films grown on perovskite substrates are important building blocks for catalytic and electronic materials systems. This includes use as heterogeneous catalysts,[1,2] ferroelectric devices,[3] giant magnetoresistance thin films,[4] and tunable microwave capacitors.[5] One such metal/perovskite heterostructure is Pt/$SrTiO_3$. This system attracts great attention because Pt has high electrical conductivity and excellent thermal stability against oxidation, and $SrTiO_3$ (STO) is a model system representing a large class of oxides with the perovskite structure.[6–8] However, for this system and its technological applications, a key question is how to effectively control the properties of the metallic film, such as surface morphology (3D particles or conformal film growth),[9,10] crystallinity, and grain size.[11]

At room temperature Pt has a face-centered cubic crystal structure with lattice constant $a_{Pt} = 3.924$ Å and $SrTiO_3$ has a primitive cubic crystal structure with $a_{STO} = 3.905$ Å. This close lattice match is one of several factors affecting the crystalline properties of Pt grown on $SrTiO_3$(001). Other factors are the TiO_2 or SrO termination of the $SrTiO_3$ surface,[12] deposition method, and annealing treatment. It is reported that pulsed laser deposition produces Pt films on $SrTiO_3$(001) with nearly perfect cube-on-cube epitaxy for growth at 600 °C, but not at 400 °C.[13,14] For the case of dc sputtering, pre-annealing of the $SrTiO_3$(001) substrates strongly affects the crystalline orientation of the Pt films.[15] Electron beam lithography can create a Pt nano-array.[16] Pt nanoparticles can be formed either by self-assembly methods[17] or atomic layer deposition (ALD).[18–20] Compared with other growth methods, ALD has the advantage of applicability for uniformly coating granular and porous materials.

In an earlier study[19] we concentrated on the nucleation and growth of as-deposited (AD) ALD Pt on single crystal $SrTiO_3$(001) surfaces as a function of number of ALD cycles in the Pt coverage range of 1 to 40 monolayers (ML). Because ALD is a low-temperature growth method, these AD surfaces are expected to be far from equilibrium. Herein we report how post-annealing is used to drive these same surfaces closer to thermal equilibrium. The consequential structural and morphological changes are studied by a combination of x-ray and imaging techniques. Atomic force microscopy (AFM) and scanning electron microscopy (SEM) reveal that nearly continuous AD Pt films coalesce to form separated nanoparticles after a high temperature anneal. Besides these surface morphological changes, x-ray techniques also show that there is a dramatic structural change when the Pt coverage is sufficiently high. Using reciprocal space mapping and grazing-incidence small-angle x-ray scattering (GISAXS), cube-on-cube epitaxial nanocrystals were found at the 40 ML Pt coverage. These thermally induced morphological and structural changes are understood in terms of surface diffusion, surface and interface energy, and surface energy anisotropy that are related to the annealing temperature, Pt coverage, and the initial surface morphologies of the AD ALD Pt films. These findings can be applied to the growth of other noble metals on oxides and the control of their microstructure and morphologies.

II. EXPERIMENTAL

Following previously established surface preparation procedures,[6,21,22] $10 \times 10 \times 1$ mm^3 $SrTiO_3$ (001) substrates

[a)]Author to whom correspondence should be addressed. Electronic mail: bedzyk@northwestern.edu.

 © 2011 American Institute of Physics

Author complimentary copy. Redistribution subject to AIP license or copyright, see http://jap.aip.org/jap/copyright.jsp

(MTI Corp.) were solution cleaned and then dried with nitrogen gas. To obtain atomically flat TiO_2 terminated surfaces, the substrates were loaded into a tube furnace with flowing O_2 (~100 sccm) at 760 Torr and annealed at 1050 °C for 5 h. AFM, described below, showed that the surfaces had flat terraces with 4 Å steps, consistent with the $SrTiO_3$ lattice constant. The $SrTiO_3$(001) substrates were then transferred to a custom ALD reactor consisting of a hot-walled stainless steel tube and a computer controlled gas manifold for precursor dosing.[23] Before Pt growth the substrates in the ALD reactor were allowed to equilibrate and outgas for 10 min at 300 °C in a flowing nitrogen environment. To grow Pt by ALD, the substrates were alternatively exposed to $MeCpPtMe_3$ (Strem Chemicals, 99.5% pure) and 400 sccm of ultrahigh purity (99.995% pure) oxygen at 300 °C carried by 360 sccm of ultrahigh purity (99.995% pure) nitrogen at a steady state pressure of ~1 Torr.[21] A Pt ALD cycle is defined as a 10 s exposure to $MeCpPtMe_3$, a 5 s N_2 purge period, a 5 s exposure to O_2, and a final 5 s N_2 purge period. Our previous study of the as-deposited surfaces formed by 10 to 80 ALD cycles of Pt on STO (Ref. 21) showed that Pt nucleates as isolated islands, the islands grow laterally with repeated Pt ALD cycles, and the islands coalesce to form a nearly continuous film after 40 cycles. After 40 cycles the constant growth rate was ~0.5 Å/cycle. X-ray photoelectron spectroscopy (XPS) confirmed that the platinum chemical state was metallic for these as-deposited films.[21]

For this report $Pt/SrTiO_3$ samples were prepared using 10, 20, 30, 40, and 80 Pt ALD cycles. To study the Pt structural and morphological changes due to annealing, the ALD samples were studied in their as-deposited (AD) condition and after annealing (AN) in ultrahigh vacuum (UHV) at 800 °C for 10 min.

A Thermomicroscopes CP Research AFM operated in intermittent contact mode was used to collect surface morphology information from all surfaces discussed in this study. The silicon AFM tips (μMasch) had a nominal 10 nm radius of curvature and resonant frequency of ~70 kHz. The piezo tube motion was corrected by a polynomial subtraction to the images. The vertical piezo response was calibrated using standard $SrTiO_3$(001) ($d_{001} = 3.905$ Å) and TiO_2(110) ($d_{110} = 3.25$ Å) samples.

SEM imaging was performed using a Hitachi S-4800 II cFEG SEM. The samples were imaged in the SEM without the use of conductive coatings.

The Pt coverage was measured by x-ray fluorescence (XRF) using a Zr coated rotating anode and an energy-dispersive XRF detector at the Northwestern University (NU) X-ray Facility. The 15.75 keV Zr Kα x-rays excited Pt L fluorescence without inducing Sr K fluorescence, which would have saturated the XRF detector system. The Pt Lα XRF yield from each ALD deposited film was converted into a Pt coverage by using a side-by-side comparison to a Rutherford backscattering calibrated Pt standard. For the $SrTiO_3$(001) surface, 1 monolayer (ML) corresponds to $N_{surface}^{STO} = a_{STO}^{-2} = 6.558$ atoms/nm^2.

X-ray reflectivity (XRR) and reciprocal space map data were collected with Cu Kα_1 ($\lambda = 1.5406$ Å) radiation from rotating anode-based diffractometers in the NU X-ray Facility. A Rigaku ATX-G with a parabolic multilayer followed by a Ge(111) condenser-two-bounce monochromator was used for XRR and a Huber 4-circle with a graphite sagittal focusing monochromator was used for collecting the reciprocal space maps. The reflectivity data as a function of scattering angle 2θ was background subtracted, dead time corrected, and normalized to the straight-through beam intensity. The low-angle XRR data as a function of perpendicular momentum transfer $Q = Q_Z = 4\pi \sin\theta/\lambda$ was fitted by the Motofit program, which uses a slab-model approach with Parratt's recursion formulation to perform dynamical scattering analysis.[24]

GISAXS measurements were performed at the XOR 12ID-C at the Advanced Photon Source (APS; Argonne National Laboratory) with a 2048×2048 pixel MAR165 CCD detector. The incident photon energy was 11.50 keV. The sample-to-detector distance was 2 m. Samples were mounted on a two-circle diffractometer that enabled rotations to set the incident angle, α_i, and azimuthal rotation angle, ϕ, about the substrate surface normal. While samples were measured at various incident angles, GISAXS data presented in this report were collected with $\alpha_i < \alpha_C$; where $\alpha_C = 0.15°$ is the critical angle of the $SrTiO_3$ substrate. This corresponds to $Q_C = 0.032$ Å^{-1}. A silver behenate standard was used for angle calibration, and images were corrected for detector dark current via data subtraction.

III. RESULTS AND DISCUSSION

Figure 1 and Table I present the AFM analysis illustrating the evolution of the $Pt/SrTiO_3$(001) surface morphological changes before and after the 800 °C UHV anneal. Each starting blank $SrTiO_3$(001) surface (not shown) was atomically flat with an RMS roughness of 0.1 nm. The XRF determined Pt coverage for each sample is listed in Table I. We showed previously that the ALD Pt forms a uniform coating of isolated nanoparticles on the $SrTiO_3$(001) surface in the early stages of growth.[21] Consistent with this observation, terraces were still clearly seen after ALD via AFM, indicating a conformal film-like structure on the surface. The rms roughness of the AD samples increased only slightly with the number of ALD cycles. However, after annealing, the AFM images show distinctive morphological changes for higher coverages. Figure 1(a) shows a 0.2 nm rms roughness for the 0.7 ML AN sample, indicating that annealing has little effect at low Pt coverages. As more Pt is deposited, annealing has a stronger effect. As shown in Figs. 1(b)–1(e), the 0.4 nm atomic steps that were preserved on the AD surfaces disappear in the images of the annealed surfaces as the Pt starts to coalesce. The Pt coalescence and average cluster size increase with Pt coverage resulting in an increased roughness.

Figure 2 shows the SEM images of the annealed samples with 20, 40, and 80 ALD cycles. Compared to our earlier reported SEM images of similarly prepared as-deposited samples,[21] the Pt nanoparticles become significantly larger after annealing. The SEM observation that the 80-cycle sample shows the most dramatic size increase effect confirms the AFM observations of Fig. 1 that annealing has a much

Author complimentary copy. Redistribution subject to AIP license or copyright, see http://jap.aip.org/jap/copyright.jsp

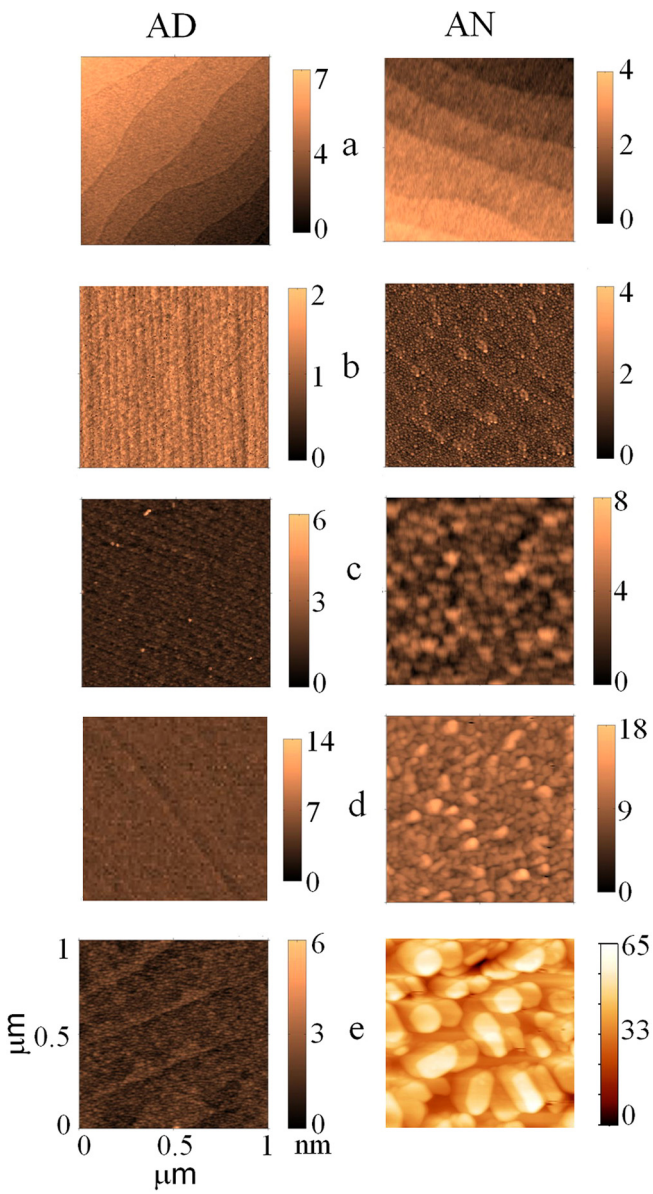

FIG. 1. (Color online) Pairs of 1×1 μm^2 AFM images for ALD Pt on $SrTiO_3$(001). The left-hand column shows the images for the as-deposited (AD) surfaces. The right-hand column shows the same surfaces after annealing (AN) to 800 °C in UHV. The number of ALD cycles for each pair of images is: (a) 10, (b) 20, (c) 30, (d) 40, and (e) 80. The 0.4 nm atomic steps of the underlying $SrTiO_3$ (001) substrate are clearly seen for all AD surfaces and for the 10-cycle AN surface.

stronger effect for surfaces with a higher Pt coverage. Furthermore, as seen in Fig. 2(c), the Pt nanoparticles of the AN 80-cycle sample show faceted edges.

To better understand the film and interfacial properties, XRR analysis was carried out as shown in Fig. 3 on the AD films. The results are summarized in Table II. The thickness fringes in the XRR data confirm the conformal film-like structure of the AD samples. However, the XRR determined effective electron density (ρ_{film}) for each film is less than that of bulk Pt ($\rho_{bulk} = 5.164$ Å^{-3}). Table II shows that the 20-cycle sample has only 60% of the bulk Pt electron density, while the other cases have roughly 80%. The XRR fit uses a slab model that assumes a homogenous density for the

TABLE I. XRF determined Pt coverage (Θ_{XRF}) and AFM measured rms roughness for the set of ALD Pt/$SrTiO_3$(001) surfaces. AD = as-deposited surface. AN = annealed surface. Prior to ALD the AFM surface rms roughness was 0.1 nm.

ALD cycles	(Θ_{XRF}) (ML)	AD rms (nm)	AN rms (nm)
10	0.7	0.21	0.16
20	11.2	0.22	0.47
30	25.1	0.31	0.97
40	35.6	0.45	1.65
80	39.8	0.91	7.57

Pt layer. The laterally averaged value being less than bulk Pt density is consistent with Pt forming a discontinuous film. The real Pt distribution could be more complicated, such as Pt islands on a fully covered Pt layer. Table II also shows that the Pt coverages determined from XRR (Θ_{XRR}) are consistent with those determined from XRF (Θ_{XRF}) in Table I.

Typically for metals grown on oxides, there are three different growth modes, namely, (1) layer-by-layer or Frank-van der Merwe (F-M) growth, (2) three-dimensional islands or Volmer-Weber (V-W) growth, and (3) intermediate case of three-dimensional islands on layered films or Stranski-Krastanov (S-K) growth.[25,26] Our XRR analysis of the AD ALD Pt films is consistent with the S-K and/or V-W growth mode with 2D discontinuous films instead of 3D islands. This is also confirmed from images taken by AFM (Fig. 1) and SEM in previous studies.[21] At low temperature (300 °C in ALD) a "2D island" mode[27] can dominate and consequently 2D films can be observed.

For all these AD samples, no Pt Bragg peaks were observed at higher Q, indicating these AD films have crystal domains with sizes below the ~10 nm detectable limit for our rotating-anode x-ray source with single crystal substrates. [See Fig. 4(b)] Note that for 1 to 5 ALD Pt cycles on single crystal STO nanocubes with {001} faces that the AD Pt formed fcc nanocrystals[20] with cube-on-cube epitaxy.[28] For these powder samples, with a much larger effective surface area, synchrotron-based XRD measurements observed high-Q diffraction peaks with widths corresponding to domain sizes between 1 and 3 nm.

After UHV annealing, the low-Q reflectivity for each of these samples shows a significant change that becomes more dramatic as the Pt coverage increases. Figure 4(a) shows the reflectivity change for the 80-cycle sample before and after annealing. At lower Q, no thickness fringes were observed, indicating that the conformal film feature was lost. However at higher $Q = Q_Z$, as shown in Fig. 4(b), a Pt (002) peak appears. This indicates that the annealing-induced clusters seen in Fig. 1(e) by AFM and in Fig. 2(c) by SEM are Pt ordered nanocrystals with preferred (001) orientation along the surface normal direction. Annealing further breaks up the already discontinuous microstructural film causing it to aggregate (coarsen) into larger more separated clusters, as seen in Fig. 1 and Fig. 2. Figures 4(c) and 4(d) are reciprocal space maps surrounding the $SrTiO_3$ (111) and (002), respectively. This shows strain-relaxed Pt with $[111]_{Pt} \parallel [111]_{STO}$ and $[001]_{Pt} \parallel [001]_{STO}$, indicating that Pt nanocrystals have a

Author complimentary copy. Redistribution subject to AIP license or copyright, see http://jap.aip.org/jap/copyright.jsp

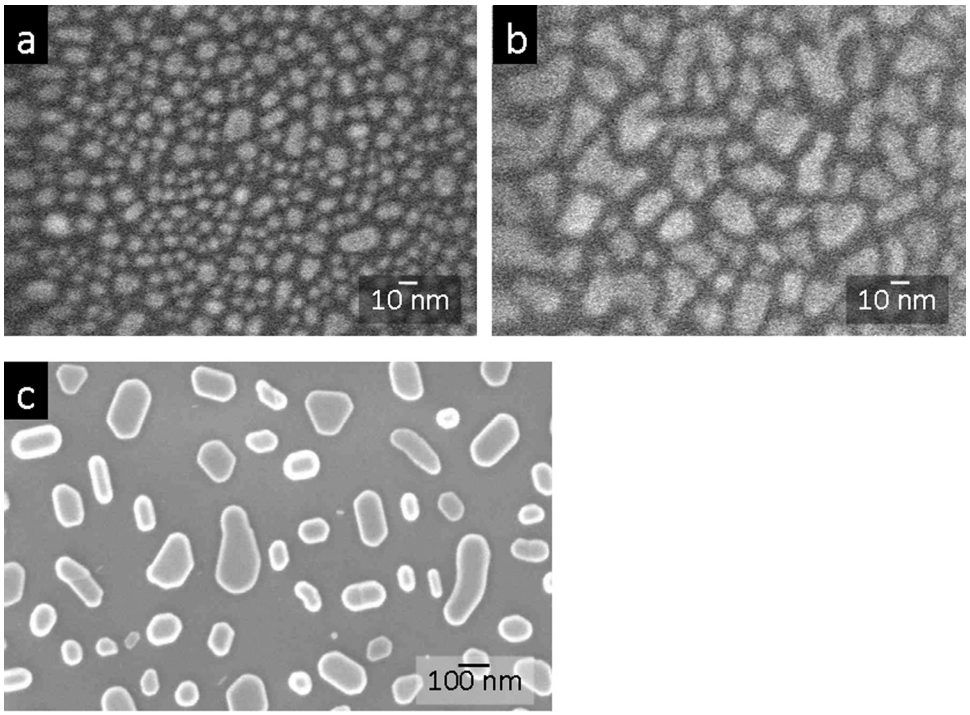

FIG. 2. High-resolution SEM images for ALD Pt/$SrTiO_3$(001) after annealing: (a) 20 cycles, (b) 40 cycles, and (c) 80 cycles. Aggregation is greatly enhanced for the 80-cycle sample, in which faceting can be seen.

cube-on-cube epitaxial structure on $SrTiO_3$(001) after annealing. Analysis of the Pt (002) and (111) Bragg peaks shows a bulk-like lattice of $a = 3.92$ Å with peak widths (corrected for the 0.007 $Å^{-1}$ instrument resolution) of $\Delta Q_z = 0.043$ $Å^{-1}$ and $\Delta Q_{xy} = 0.036$ $Å^{-1}$ corresponding to Pt nanocrystal domain sizes of 14 nm in the vertical and 16 nm in the horizontal directions, respectively. Note that this Pt (002) Bragg peak was below the detection limit for similar radial scans of the other annealed ALD samples. As seen in the AFM and SEM images, Pt nanoparticles sizes change dramatically from low coverages to higher coverages. The typically larger nanoparticles seen by AFM and SEM contain smaller ordered crystal domains as measured by high-Q XRR. As the Pt coverage increases, the sizes of both nanoparticles and the ordered crystal domains increase after annealing.

To further understand the morphological changes, GISAXS measurements were carried out for the 10, 20, 30, and 40 ALD-cycle samples in the AD and AN states. As a representative example, Fig. 5 shows the GISAXS data for the 10-cycle sample before Pt deposition, after deposition, and after annealing. Figure 5(a) shows the expected scattering from an atomically flat surface where the majority of the intensity remains in the specular direction and is blocked by the beamstop. In contrast, Figs. 5(b) and 5(c) show the characteristic scattering of closely spaced polydispersed particles that are monolayered; with a broad peak along the in-plane (Q_{xy}) direction and with a monotonically decaying intensity along the vertical (Q_z) direction. Comparing Figs. 5(b) and 5(c), the scattered intensity condenses around the origin. This indicates very small, closely spaced particles coalescing into larger particles that are spaced farther apart. Using the analysis in our previous work,[21] the horizontal and vertical line cuts of intensity were extracted from the CCD images and fit using the distorted wave Born approximation[29,30] (DWBA) framework for a cylinder form factor and the local monodisperse approximation[29,31] (LMA) with 1D paracrystal model[29] for an interference function representing the interparticle spacing distribution. Figure 6 shows the vertical

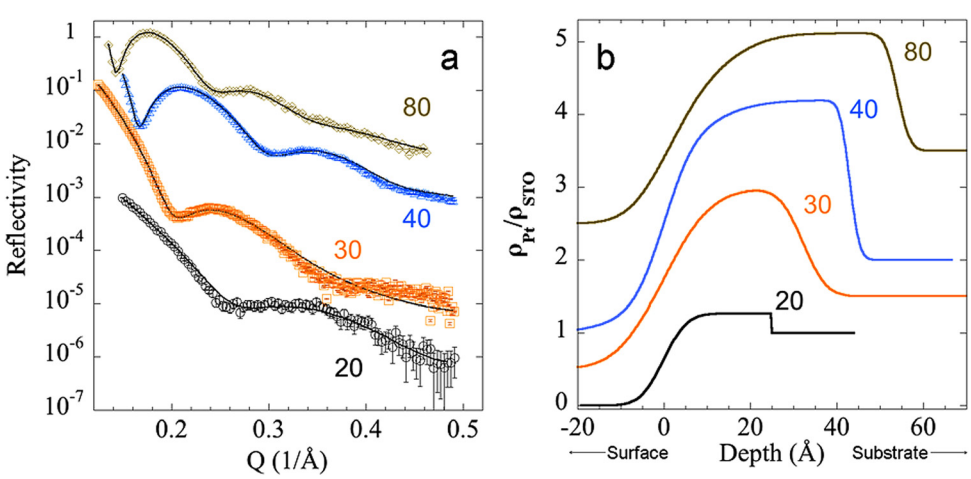

FIG. 3. (Color online) (a) XRR data and analyses for as-deposited (AD) ALD Pt/$SrTiO_3$(001) thin film samples. (b) The electron density profiles that were determined by the best fit of a model to each set of XRR data. Curves are offset vertically for purposes of clarity. The number next to each curve represents the number of ALD cycles. See Table II for the values of the fit determined parameters.

Author complimentary copy. Redistribution subject to AIP license or copyright, see http://jap.aip.org/jap/copyright.jsp

TABLE II. Summary of XRR data analyses shown in Fig. 2 for the as-deposited ALD Pt/$SrTiO_3$(001) interfaces: Pt film thickness (t), film electron density relative to bulk Pt ($\rho_{film}/\rho_{\mathrm{bulk}}$), and XRR determined Pt coverage $\Theta_{XRR} = \frac{\rho_{film}}{\rho_{bulk}^{Pt}} N_{bulk}^{Pt} \frac{t_{film}}{N_{Surface}^{STO}}$, where $N_{bulk}^{Pt} = 4a_{Pt}^{-3} = 66.20\ \mathrm{nm}^{-3}$ and $N_{surface}^{STO} = a_{STO}^{-2} = 6.558\ \mathrm{nm}^{-2}$.

ALD cycles	t_{film} (nm)	$\rho_{film}/\rho_{\mathrm{bulk}}$	Θ_{XRR} (ML)
20	2.3 ± 0.2	0.56 ± 0.19	13 ± 5
30	3.2 ± 0.1	0.79 ± 0.11	25 ± 4
40	4.3 ± 0.1	0.85 ± 0.04	37 ± 2
80	5.4 ± 0.2	0.79 ± 0.09	43 ± 5

line cut of the data and fits, and Table III lists the analysis results for each sample. For the 10-cycle sample, there is no significant size or shape change before and after annealing. This is consistent with AFM analysis, and the GISAXS result suggests the formation of Pt nanoparticles. For samples with 20–40 ALD cycles after annealing, the in-plane nanocrystal size, R, changes dramatically, while the out-of-the-plane height, H, changes slightly. The in-plane nanocrystal size is consistent with that measured by SEM. This indicates that annealing mainly affects the lateral structure of the Pt. However, for the 80-cycle sample, XRR analysis shows that the film thickness is 5.4 nm before annealing as compared with a post-annealing 14 nm vertical domain size, which can be considered as the lower limit of the cluster height. This indicates that Pt aggregates much more strongly in the vertical direction under thermal treatment for the higher coverage sample.

The GISAXS observed annealing effects are most dramatic in the higher coverage 80 ALD cycle case shown in Fig. 7; where evidence of long-range orientational ordering and faceting of the Pt nanocrystals can be seen. These images are part of a set of GISAXS patterns collected at 2° intervals in azimuthal angle ϕ over a range of 180°. Figure 7(a) was taken with the incident beam approximately along the $SrTiO_3$ [100] direction; whereas Fig. 7(b) was along the [100]. This rotation shows a change in the intensity pattern consistent with scattering from nanoparticle crystallographic facets.[29] In this case, a scattering lobe is directed at an angle of ∼55° from the specular direction and is fourfold symmetric about the surface normal rotation axis. This would indicate {111} facets for Pt nanoparticles with cube-on-cube epitaxy. Furthermore, the Pt nanoparticles in this case possess a high degree of long-range orientational ordering as GISAXS measures the ensemble average of nanoparticle orientation. Similar in-plane investigations for the cases of ALD cycles less than 80 yielded no such evidence of faceting or long-range orientational ordering. The four-fold symmetric GISAXS intensity about the surface normal indicates a pyramidal or truncated pyramidal nanocrystal morphology with {111} facets.[29] The SEM image in Fig. 2(c) shows a morphology in which the nanocrystals appear to be faceted and exhibit an in-plane directional edge pattern that is not simply fourfold symmetric. This seeming discrepancy between GISAXS and SEM could be due to the fact that many of the nanoparticles as observed by SEM are elongated and stretch at regular angles across the surface; while GISAXS senses the ensemble averaged structure. However, for lower Pt coverage, i.e., ALD cycles less than 40, no faceting of the Pt nanocrystals was observed. These results indicate that the UHV annealing has stronger effects on high coverage Pt and therefore a

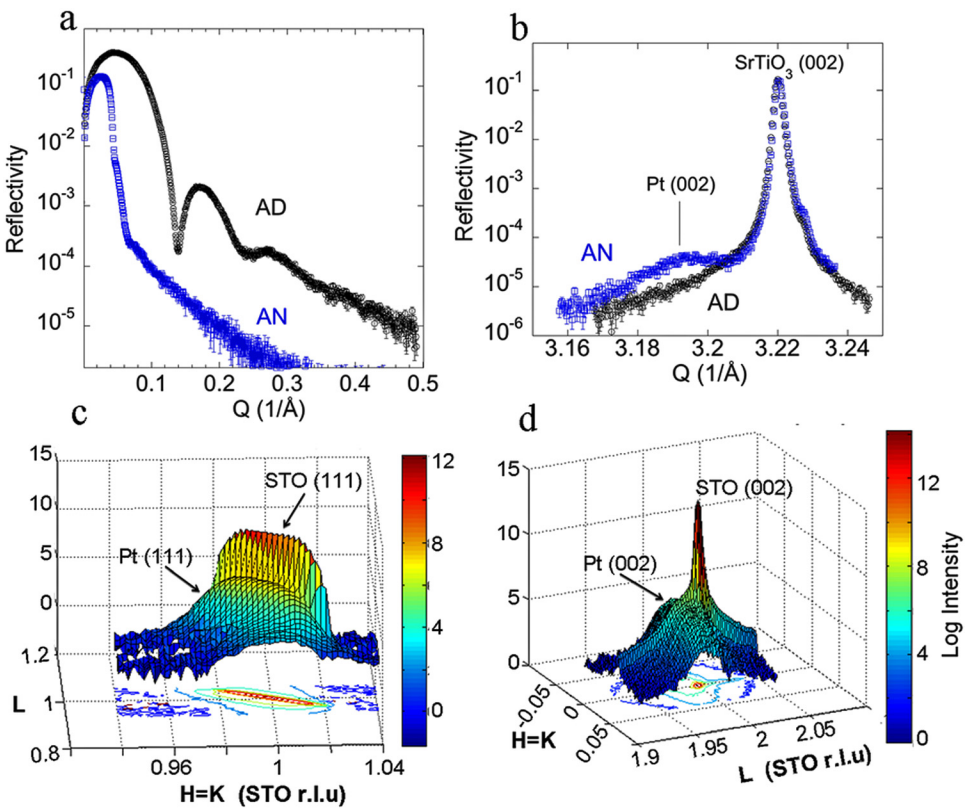

FIG. 4. (Color online) For 80 cycles ALD Pt/$SrTiO_3$(001) sample: (a) Low-Q and (b) high-Q XRR data for AD (black circles) and AN (blue square) conditions. Reciprocal space maps and contour plots using $SrTiO_3$ (STO) reciprocal lattice units (r.l.u.) in the vicinity of (c) (111) and (d) (002). Note that in (a) the critical angle for bulk-like $SrTiO_3$ and Pt correspond to $Q_C = 0.032$ and 0.084 $Å^{-1}$, respectively.

Author complimentary copy. Redistribution subject to AIP license or copyright, see http://jap.aip.org/jap/copyright.jsp

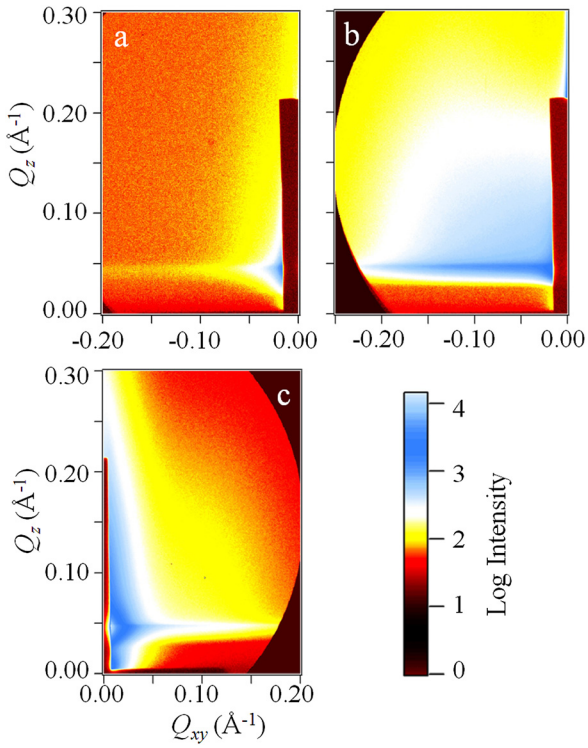

FIG. 5. (Color online) GISAXS data for (a) blank atomically flat $SrTiO_3$ (001) surface, (b) 10 ALD cycles Pt as-deposited and (c) 10 ALD cycles Pt after 800 °C UHV annealing.

structural correlation between the platinum and strontium titanate can be observed.

These various annealing effects of Pt with different coverages can be attributed to surface diffusion, interfacial energy, and surface energy anisotropy of noble metals (including platinum, gold, and palladium) on oxide surfaces. The typical thermodynamic preference of metal/ceramic systems is to leave exposed substrate surface and form 3D island-like morphologies.[13] However, at low temperatures

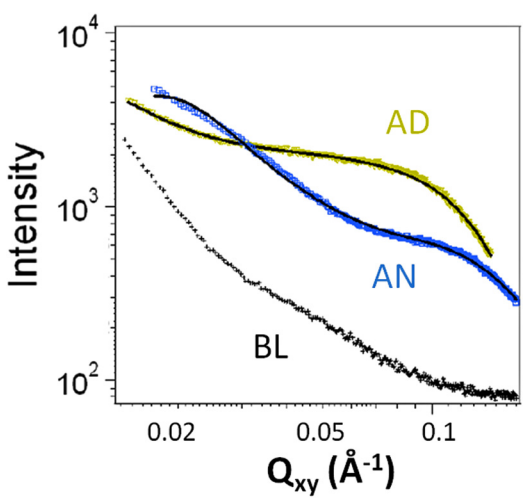

FIG. 6. (Color online) GISAXS horizontal line cut data and fits for blank (BL) $SrTiO_3$, Pt 10 cycles ALD as deposited (AD), and after annealing (AN). The individual curves are vertically offset for clarity. The line cuts are taken at $Q_Z = 0.04$ Å^{-1}. The values of the fit determined parameters are listed in Table III.

TABLE III. GISAXS fitting and analysis results for as-deposited (AD) and annealed (AN) ALD $Pt/SrTiO_3(001)$ samples. In this case, the particle model is taken to be a cylinder of radius, R, and height, H, with a center-to-center interparticle spacing, D. The parameter, σ, gives the distribution width of the respective parameter.

ALD cycles	R (nm)	σ_R (nm)	H (nm)	σ_H (nm)	D (nm)	σ_D (nm)
AD						
10	1.1	0.1	1.2	0.3	2.2	0.8
20	2.1	0.5	2.3	0.6	6.3	1.3
30	3.1	0.7	3.0	0.8	9.0	2.1
40	3.5	0.9	3.8	1.0	9.0	2.5
AN						
10	1.2	0.1	1.0	0.1	2.6	0.7
20	3.4	0.9	3.3	0.4	9.9	0.3
30	6.9	2.6	4.1	0.6	21.4	0.7
40	9.0	3.0	4.3	0.7	37.8	0.7

island growth cannot be reached. Therefore a "quasi-2D" or "2D island" growth mode[27] dominates and flat metal films can be gown.[32,33] This would be consistent with the discontinuous films (2D islands) we observed for the AD Pt films grown at 300 °C. When annealed at a higher temperature (800 °C), Pt adatoms gain sufficient kinetic energy to diffuse on the surface, causing the formation of nanoparticles. The strong temperature-dependent effect of Pt surface diffusion coefficient in cm^2/s is described by an empirical relationship given by Gjostein,[34]

$$D_s(T) = 0.014 \exp\left(-\frac{13T_m}{R_c T}\right), \quad (1)$$

where T and T_m are the substrate temperature and Pt melting point in °K, and $R_c = 1.99$ cal mol^{-1} K^{-1} is the gas constant. This surface diffusion coefficient at 800 °C is 5.8×10^{-8} cm^2/s, much greater than that at 300 °C, 1.2×10^{-12} cm^2/s. For sub-monolayer coverages, Pt on $SrTiO_3(001)$ surfaces exists as widely separated nanoparticles, which under thermal treatment may come together without sintering to form larger nanoparticles.[21] It is also possible that under UHV annealing these widely distributed Pt nanoparticles are encapsulated by the substrate titanium oxide layers,[35] prohibiting Pt mobility at high temperature. Therefore in this sub-monolayer case after annealing, no significant surface structural changes were observed by GISAXS, which is most sensitive to small nanoparticles. However, as the Pt coverages increase, high surface diffusion and limited surface area cause Pt to come together. In another view, encapsulation of Pt nanoparticles by the substrate cannot compete with Pt coalescence, also resulting in the formation of larger nanoparticles.

In addition to surface diffusion, the interfacial energy and the surface energy anisotropy, or the difference between the surface energies of competing metal film orientations, also play important roles in determining the surface morphology and Pt nanoparticles orientations. Generally speaking, epitaxial orientation minimizes the surface and interface energy.[12] Growth of (001)-orientated fcc metals on oxides is challenging because close-packed {111} planes have the

Author complimentary copy. Redistribution subject to AIP license or copyright, see http://jap.aip.org/jap/copyright.jsp

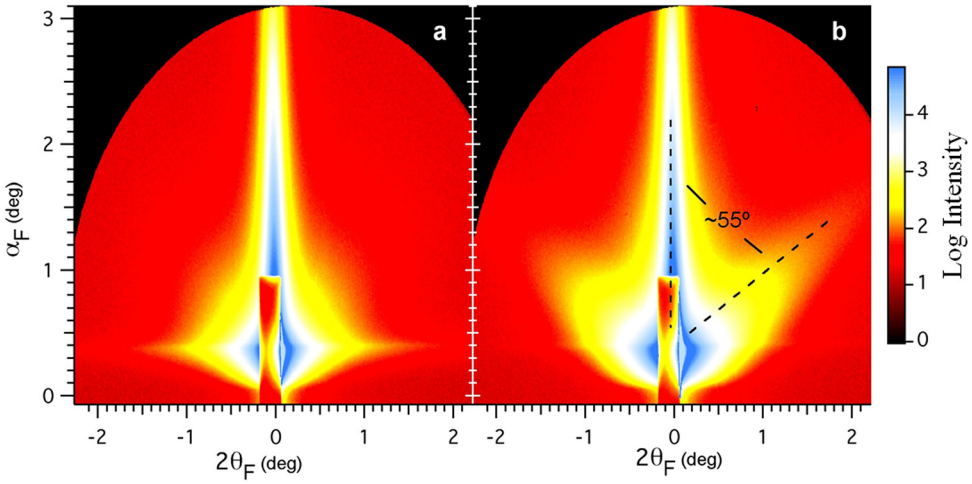

FIG. 7. (Color online) GISAXS data showing faceting and long-range orientational ordering of the Pt nanocrystals for the annealed 80 ALD cycle case. The data is given as a function of scattering angles α_F and $2\theta_F$ for simplicity. Pattern (a) was collected with the incident beam approximately along the $SrTiO_3$ [100] direction; while (b) was taken along the [110] direction. The intensity lobe in (b) is indicative of scattering off the {111} facet for a Pt nanocrystal with cube-on-cube epitaxy.

lowest relative surface energy, γ.[36,37] From powder diffraction studies of 20 to 110 nm thick platinum films grown via ALD on amorphous substrates, {111} texture was strongly preferred.[18] To achieve (001)-orientated films, this energetic preference must be overcome by a favorable interfacial relationship between the ceramic and the metal (001) orientation. Furthermore, because Pt has low oxygen affinities, for growth temperature $T < 600\,^{\circ}C$, various crystal orientations can be expected.[14] When these samples were annealed at 800 °C, the AD ALD Pt with discontinuous film structures started to coalesce, forming 3D islands, as observed in AFM and SEM. This aggregation can be understood as an Ostwald ripening process, which is also observed for other noble metals grown on oxides, such as $Ag/TiO_2(110)$,[38] $Au/TiO_2(110)$,[39] and $Au/FeO(111)$.[40] In our case, discrete Pt nanoparticles formed at sub-monolayer are not measurably affected by annealing, showing some thermodynamic stabilization. However, when the sample coverages are in excess of several ML, formation of large nanoparticles is the dominant trend, although some very small nanoparticles are still visible, as seen by SEM. This bimodal size distribution[38,39] of Pt nanoparticles is the evidence for Ostwald ripening, which is observed as some particles increase in size while other particles shrink.

The formation of (001)-orientated epitaxial nanocrystals at a higher Pt coverage can be explained by the temperature dependence of Pt surface anisotropy, $\gamma(001)/\gamma(111)$. At high temperature (800 °C in our case), the Pt surface energy anisotropy is lowered and the energetic preference to {111} planes thus becomes lower, while the film/substrate interfacial energy is unaffected.[13] This will promote the epitaxial (001) orientation of Pt on $SrTiO_3(001)$. On the other hand, fast surface diffusion at high temperature means that atoms can most easily locate their preferred crystalline orientation.[14] In our ALD Pt samples, only the higher coverage sample, 80 ALD cycles, achieved detectable epitaxy. This is because the initial Pt grain size and the initial degree of surface coverage are also primary factors in determining the epitaxial growth, as shown elsewhere.[41] Monte Carlo simulations show that high initial Pt coverages result in the growth of the epitaxial grain sizes and can eventually evolve to an epitaxial thin film, while low initial Pt coverage can only result in a final polycrystalline microstructure.[41] This is consistent with our observation. For coverages lower than 40 ML, some Pt epitaxial grains may form, but not sufficiently enough to form larger ordered nanocrystal domains above our ~10 nm detectable limit. When the Pt coverage is sufficiently high, as with the 80 ALD cycle case, Pt aggregates more in the vertical direction during the annealing process, and eventually results in the formation of strain-relaxed Pt nanocrystals with cube-on-cube epitaxial structure. The formation of the faceted Pt nanocrystals is complicated. As shown in the $Pt/Al_2O_3(0001)$ case,[42] faceting was observed at some critical thickness by AFM. Several factors can affect this formation, such as surface and edge diffusion,[43] elastic interaction,[44] and substrate interaction.[45] As a result of various defect sites and different substrate terminating atoms, the surface energy can vary by up to 30%.[46] For a particular initial film thickness, the Pt surface can exhibit varying diffusivity, leading to a wide range of geometric shapes.[42] In our case, the coupling and competition of the above factors result in Pt {111} faceting.

IV. CONCLUSIONS

In this work, we studied the thermally induced nanoscale nucleation and structural changes of Pt on $SrTiO_3(001)$ synthesized by ALD with 20 to 80 growth cycles. Combined AFM, SEM, XRF, XRR, reciprocal space map, and GISAXS measurements show that Pt exhibits different structural and surface morphological changes after annealing that depend on the initial as-deposited Pt coverage in the range of 1 to 40 ML. This is attributed to the surface diffusion, interfacial energy, and surface energy anisotropy of noble metals on oxide surfaces. Annealing has no significant effect on widely separated Pt nanoparticles formed at sub-monolayer coverages, while it causes aggregation for Pt films formed at coverages exceeding several monolayers. This effect becomes stronger for thicker Pt (i.e., more than 40 ALD cycles) that changes from a film with no observable texture to {111} faceted nanocrystals with cube-on-cube epitaxy. This thermal-induced aggregation and crystallization with respect to the substrate lattice should motivate future studies for the nucleation of noble metals grown by atomic-layer deposition.

Author complimentary copy. Redistribution subject to AIP license or copyright, see http://jap.aip.org/jap/copyright.jsp

ACKNOWLEDGMENTS

This work was supported by the Institute for Catalysis in Energy Processes at Northwestern University [U.S. Department of Energy (DOE) under contract DE-FG02-03ER15457]. Measurements were performed at the Advanced Photon Source and the Electron Microscopy Center, which are supported at Argonne National Laboratory by the U.S. Department of Energy (DOE) under contract DE-AC02-06CH11357 to the University of Chicago Argonne, LLC. This work made use of Northwestern University Central Facilities supported by the Materials Research Science and Engineering Center through National Science Foundation (NSF) under contract DMR-0520513. The authors are also thankful for technical assistance from Robin Koshy, Michael Graham, and Jerrold Carsello.

[1]R. G. Carr and G. A. Somorjai, Nature **290**, 576 (1981).
[2]M. Kitano and M. Hara, J. Mater. Chem. **20**, 627 (2010).
[3]O. Auciello, J. F. Scott, and R. Ramesh, Phys. Today **51**, 22 (1998).
[4]C. N. R. Rao, Philos. Trans. R. Soc. London Ser. A **356**, 23 (1998).
[5]A. K. Tagantsev, V. O. Sherman, K. F. Astafiev, J. Venkatesh, and N. Setter, J. Electroceram. **11**, 5 (2003).
[6]M. Kawasaki, K. Takahashi, T. Maeda, R. Tsuchiya, M. Shinohara, O. Ishiyama, T. Yonezawa, M. Yoshimoto, and H. Koinuma, Science **266**, 1540 (1994).
[7]R. Herger, P. R. Willmott, O. Bunk, C. M. Schlepuetz, B. D. Patterson, and B. Delley, Phys. Rev. Lett. **98**, 076102 (2007).
[8]T. Matsumoto, H. Tanaka, T. Kawai, and S. Kawai, Surf. Sci. **278**, L153 (1992).
[9]M. M. Nowell and D. P. Field, Mater. Res. Soc. Symp. Proc. **1998**, 115 (1998).
[10]G. S. Was, D. J. Srolovitz, and D. Liang, Mater. Res. Soc. Symp. Proc. **1997**, 311.
[11]A. Gungor, K. Barmak, A. D. Rollett, C. Cabral, and J. M. E. Harper, J. Vac. Sci. Technol. B **20**, 2314 (2002).
[12]A. D. Polli, T. Wagner, T. Gemming, and M. Ruhle, Surf. Sci. **448**, 279 (2000).
[13]A. J. Francis, Y. Cao, and P. A. Salvador, Thin Solid Films **496**, 317 (2006).
[14]A. J. Francis and P. A. Salvador, J. Mater. Res. **22**, 89 (2006).
[15]J. Son, J. Cagnon, and S. Stemmer, J. Appl. Phys. **106**, 043525 (2009).
[16]V. Komanicky, K. C. Chang, A. Menzel, D. Hennessy, G. Karapetrov, and H. D. You, Sol. Hydrogen Nanotechnol. **6340**, U278 (2006).
[17]V. Komanicky, A. Menzel, K. C. Chang, and H. You, J. Phys. Chem. B **109**, 23543 (2005).
[18]T. Aaltonen, M. Ritala, T. Sajavaara, J. Keinonen, and M. Leskela, Chem. Mater. **15**, 1924 (2003).
[19]S. T. Christensen, J. W. Elam, B. Lee, Z. Feng, M. J. Bedzyk, and M. C. Hersam, Chem. Mater. **21**, 516 (2009).
[20]S. T. Christensen, J. W. Elam, F. A. Rabuffetti, Q. Ma, S. J. Weigand, B. Lee, S. Seifert, P. C. Stair, K. R. Poeppelmeier, M. C. Hersam, and M. J. Bedzyk, Small **5**, 750 (2009).
[21]S. T. Christensen, B. Lee, Z. X. Feng, M. C. Hersam, and M. J. Bedzyk, Appl. Surf. Sci. **256**, 423 (2009).
[22]G. Koster, G. Rijnders, D. H. A. Blank, and H. Rogalla, Physica C **339**, 215 (2000).
[23]J. W. Elam, M. D. Groner, and S. M. George, Rev. Sci. Instrum. **73**, 2981 (2002).
[24]A. Nelson, J. Appl. Crystallogr. **39**, 273 (2006).
[25]V. E. Henrich and P. A. Cox, *The Surface Science of Metal Oxides* (Cambridge University Press, Cambridge, England, 1994).
[26]J. A. Venables, *Introduction to Surface and Thin Film Processes* (Cambridge University Press, Cambridge, England, 2000).
[27]J. H. Van der Merwe, Interface Sci. **1**, 77 (1993).
[28]J. A. Enterkin, K. R. Poeppelmeier, and L. D. Marks, Nano Lett. **11**, 993 (2011).
[29]R. Lazzari, J. Appl. Crystallogr. **35**, 406 (2002).
[30]K. Jacobi, M. Gruyters, P. Geng, T. Bitzer, M. Aggour, S. Rauscher, and H. J. Lewerenz, Phys. Rev. B **51**, 5437 (1995).
[31]J. S. Pedersen, J. Appl. Crystallogr. **27**, 595 (1994).
[32]C. Gatel, P. Baules, and E. Snoeck, J. Cryst. Growth **252**, 424 (2003).
[33]T. Wagner, G. Richter, and M. Ruhle, J. Appl. Phys. **89**, 2606 (2001).
[34]N. A. Gjostein, in *Surfaces and Interfaces*, edited by J. J. Burke, N. L. Reed, and V. Weiss (Syracuse University Press, Syracuse, NY, 1976), pp. 271–304.
[35]O. Dulub, W. Hebenstreit, and U. Diebold, Phys. Rev. Lett. **84**, 3646 (2000).
[36]C. L. Liu, J. M. Cohen, J. B. Adams, and A. F. Voter, Surf. Sci. **253**, 334 (1991).
[37]L. Vitos, A. V. Ruban, H. L. Skriver, and J. Kollar, Surf. Sci. **411**, 186 (1998).
[38]X. F. Lai and D. W. Goodman, J. Mol. Catal. A: Chem. **162**, 33–50 (2000).
[39]C. E. J. Mitchell, A. Howard, M. Carney, and R. G. Egdell, Surface. Sci. **490**, 196 (2001).
[40]D. E. Starr, S. K. Shaikhutdinov, and H. J. Freund, Top. Catal. **36**, 33 (2005).
[41]A. J. Francis, C. G. Roberts, Y. Cao, A. D. Rollett, and P. A. Salvador, Acta Mater. **55**, 6159 (2007).
[42]D. Aurongzeb, J. Appl. Phys. **102**, 064302 (2007).
[43]C. P. Flynn, Phys. Rev. B **73**, 155417 (2006).
[44]G. Prevot and B. Croset, Phys. Rev. B **74**, 235410 (2006).
[45]A. Asthagiri and D. S. Sholl, Phys. Rev. B **73**, 125432 (2006).
[46]A. Marmier and S. C. Parker, Phys. Rev. B **69**, 115409 (2004).

Author complimentary copy. Redistribution subject to AIP license or copyright, see http://jap.aip.org/jap/copyright.jsp